

Effective production of gammas, positrons, and photonuclear particles from optimized electron acceleration by short laser pulses in low-density targets

M. G. Lobok,^{1,2} A. V. Brantov,^{1,2} and V. Yu. Bychenkov^{1,2}

¹*P. N. Lebedev Physics Institute, Russian Academy of Science,
Leninskii Prospect 53, Moscow 119991, Russia*

²*Center for Fundamental and Applied Research,
Dukhov Research Institute of Automatics (VNIIA), Moscow 127055, Russia*

Abstract

Electron acceleration has been optimized based on 3D PIC simulations of a short laser pulse interacting with low-density plasma targets to find the pulse propagation regime that maximizes the charge of high-energy electron bunches. This regime corresponds to laser pulse propagation in a self-trapping mode where the diffraction divergence is balanced by the relativistic nonlinearity such that relativistic self-focusing on the axis does not happen and the laser beam radius stays unchanged during pulse propagation in a plasma over many Rayleigh lengths. Such a regime occurs for a near-critical density if the pulse length considerably exceeds both the plasma wavelength and the pulse width. Electron acceleration occurs in a traveling cavity filled with a high-frequency laser field and a longitudinal electrostatic single-cycle field (“self-trapping regime”). Monte Carlo simulations demonstrated a high electron yield that allows an efficient production of gamma radiation, electron-positron pairs, neutrons, and even pions from a catcher-target.

PACS numbers:

I. INTRODUCTION

Electron acceleration by a laser-excited plasma wakefield with a phase velocity close to the speed of light [1] is a promising source for many applications. Excitation of a wakefield is most efficient when the laser pulse length L is of the order of the plasma wavelength, $L = \lambda_p/2$ [2]. A relativistically intense laser pulse can expel plasma electrons outward to create a traveling bare ion cavity. Such a 3D wakefield structure, which has been observed in PIC (particle-in-cell) simulations, remains stable for laser pulses shorter than the plasma wavelength, $L < \lambda_p$, and the laser pulse width, $L < d$ [3]. This regime, called the “bubble” regime is now the most used base for electron acceleration and X-ray radiation sources.

We recently performed an optimization study to correctly define the density and thickness of planar low-density targets maximizing the number of high-energy electrons generated by a femtosecond laser pulse of a given intensity. The interest in such a study is related to laser production of electron bunches that can produce hard gamma quanta with an energy exceeding 1 MeV suitable for radiography of thick dense samples, electron–positron pair production, different (γ, n) reactions including neutron generation, and even light mesons (muons and pions). A high total charge of accelerated electron bunches is required for these applications to be of practical significance. In this context, studies of laser interaction with targets of a density considerably exceeding standard rarefied gas densities (used for wakefield/bubble acceleration) [5–7] become attractive and should be advanced still further in the direction proposed in Ref. [4], where it was shown that ultrarelativistic laser pulses ($a_0 \gg 1$) of ~ 4 J energy propagating in a near-critical plasma enable acceleration of a significant number of electrons (7 nC) to an energy > 30 MeV, which could interact with bremsstrahlung converter targets and produce a desired number of gamma quanta [4]. The considered acceleration regime is quite different from a standard bubble regime with conditions opposite to Ref. [3]: $L > \lambda_p$, d [4]. Electron acceleration occurs in a traveling nonlinear 3D charge-separation structure as an elongated cavity (laser bullet) filled with a laser field and not in an empty bubble [3].

Here, we advance the study of the self-trapping regime of light propagation in a dense gas plasma to obtain the maximum yield of gammas, light elementary particles, and photonuclear reactions. The sources of X-ray radiation based on laser-triggered electrons have broad potential applications including medical and biological imaging, diagnostics for materials

science, probing of dense plasmas, and security (inspection) systems [8]. Similar sources can also be used for the strength bench test of microchips, which is important for improving the reliability of the components of electronics operating in space and safety systems. Several applications of laser-based X-ray sources have so far been demonstrated: for diagnostic radiology involving a phase-contrast imaging technique [9], for inspection relying on high-contrast gamma-ray radiography [10, 11], for production of medical isotopes via photonuclear reactions in nuclear medicine [12], for induction of photofission [13], and for the radiography of high-temperature plasmas [8]. These applications require a high brightness of the X-ray pulse generated during single laser shot. This can be achieved by increasing the number of laser accelerated electrons, and acceleration in the self-trapping regime could be the best choice.

We here extend our preliminary study of the self-trapping acceleration regime [4]. Using 3D PIC simulations, we investigate the interplay of the laser pulse and plasma parameters to choose the best parameter values for maximizing the total charge of the electron bunch produced during acceleration in the self-trapping propagation regime in a near-critical plasma. In our numerical experiment, the generated electron bunches were aimed at a bremsstrahlung converter target where their interaction leads to production of gamma pulses, electron-positron pairs, neutrons from photonuclear reaction, and more exotic particles such as light mesons, pions, and muons. The corresponding yields were calculated using the GEANT4 code.

II. SIMULATION MODEL

Here, we use 3D PIC simulations with the high-performance electromagnetic code VSim (VORPAL) to study the generation of electron bunches by a laser-generated space-charge structure from an underdense planar target represented in the form of a plasma slab of given electron density and thickness. Because we are interested in an electron beam suitable as a source for deep gamma radiography and photoproduction of neutrons and elementary particles, we choose a laser pulse that can accelerate electrons up to a typical energy (“temperature”) exceeding 100 MeV. This requires laser pulses of energies considerably higher than 1 J or sub-PW powers. For such femtosecond pulses, we study the laser-plasma interaction with low-density targets of different densities and thicknesses to find their optimum

values maximizing the number of accelerated electrons with energies of practical interest.

We consider a linearly polarized laser pulse (in the z direction) with the wavelength $\lambda = 2\pi c/\omega = 1\ \mu\text{m}$ of variable energy and a Gaussian intensity amplitude shape in time with the FWHM duration $\tau = 30\text{ fs}$ and a Gaussian amplitude profile of the focal spot with the FWHM size $D = 2R_L = 4\ \mu\text{m}$ incident along the normal to the target in the x direction. For these parameters, the standard normalized laser field amplitude $a_0 = eE_L/m_e\omega c$ was varied in the range $a_0 = 24$ to 72 , which corresponds to a maximum laser pulse intensity of $(0.8 \text{ to } 7) \times 10^{21}$ and a laser power 135 to 1200 TW. The laser pulse was focused on the front side of a plasma target consisting of electrons and heavy immovable ions. The electron densities were in the range from a few percent of the electron critical density (n_c) to a few critical densities. The target thicknesses l was varied from the pulse length $L = c\tau$ to that corresponding to almost entire pulse depletion. The simulations were performed with a moving-window technique with spatial grid steps $0.04\lambda \times 0.1\lambda \times 0.1\lambda$ in a simulation window $X \times Y \times Z = 58\lambda \times 25\lambda \times 25\lambda$.

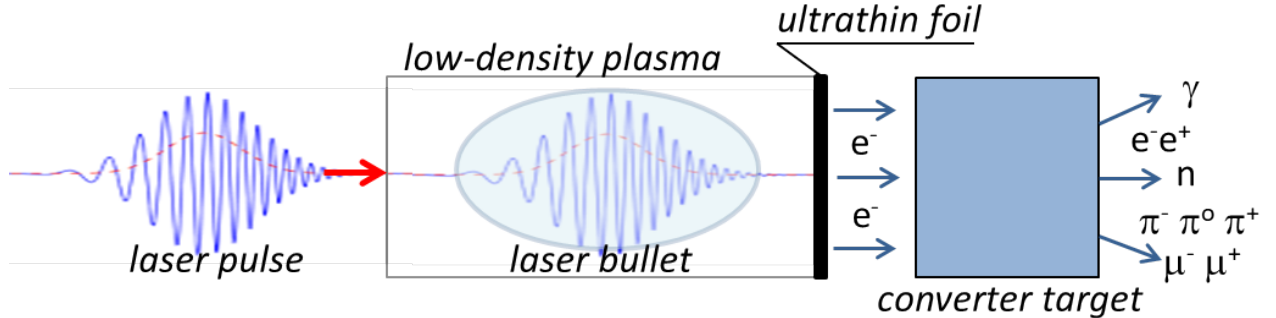


FIG. 1: Simulation laser–target layout

In our simulations, we manipulated the parameters of a planar low-density target to allow stable laser pulse propagation and effective generation of electron bunches with a high average energy and high total charge. In this study, we concentrated on studying how to accelerate as many electrons as possible. These accelerated electrons were used as an input source for further simulations of nuclear reactions in a converter target placed behind the laser target. The corresponding simulations were performed with the GEANT4 code. An ultrathin overdense plasma foil ($l = 2\ \mu\text{m}$, $n_e = 20n_c$) covered the backside of the low-density target to reflect the residual part of the laser pulse reaching the target backside; this allowed cleanly measuring the energies of free-streaming electrons without any effect

of the transmitted laser pulse. This slab entirely isolated the laser pulse from the high-Z converter target without affecting the accelerated electrons. The simulation laser-target layout is shown in Fig. 1.

III. SELF-TRAPPING REGIME

Relativistic laser pulse self-focusing and self-trapping play an important role in the stable propagation of a laser pulse over several Rayleigh lengths needed for producing high-energy, high-current electron beams inside the cavitated plasma cavern. The simulations performed clearly demonstrate the importance of matching the self-consistent waveguide radius R to the electron plasma density n_e for given laser power [14–16]. As a result of simulations, the proposed condition for matching R to n_e for indestructible pulse propagation in a relativistic plasma ($\gamma \sim a_0$) is [15, 16]

$$R \simeq \alpha \frac{c}{\omega_p} \sqrt{a_0} = \frac{c}{\omega} \sqrt{a_0 \frac{\alpha^2 n_c}{n_e}}, \quad (1)$$

where ω_p is the electron plasma frequency ($\lambda_p = 2\pi c/\omega_p$), n_c is the electron critical density for the laser frequency ω , and α is a numerical factor of the order of unity. Figure 2 from our simulations clearly shows that only a certain cavity radius for given plasma density is well suited for a stable 3D soliton-like structure filled with a high-frequency laser field (see the middle panel: $R \simeq 5\lambda \simeq 2(c/\omega_p)\sqrt{a_0}$, $n_e = 0.1n_c$, $a_0 = 24$, $R_L = 2\lambda$). Here, the laser field is shown in color, electrons are shown in gray, and the electrostatic field is shown by the dashed curve. We can use Eq. (1) to reformulate the matched laser cavern spot size condition in terms of the laser power $P = E_0^2 R^2 c/8$ as

$$R = \frac{c}{\omega} \sqrt{\frac{n_c}{n_e}} \left(\frac{16\alpha^4 P}{P_c} \right)^{1/6} \quad \text{or} \quad a_0 = \left(\frac{16P}{\alpha^2 P_c} \right)^{1/3}, \quad (2)$$

where $P_c = 2(m_e c^3/r_e)(\omega^2/\omega_p^2)$ is the critical power for relativistic self-focusing [17], $P_c \simeq 17(n_c/n_e)$ GW, and $r_e = e^2/m_e c^2$ is the classical electron radius.

We now present a simple, elegant derivation that explains matching condition (1) for the cavern spot size. We start with standard arguments usually used for a general tutorial explanation of self-focusing in a nonlinear medium. For strong cavitation, the relativistically strong electromagnetic fields in the laser focus produce an extremely high charge-separation electrostatic field expelling electrons from the laser axis and relativistically modify the electron mass such that the plasma acts as a positive lens. We apply a geometric-optical

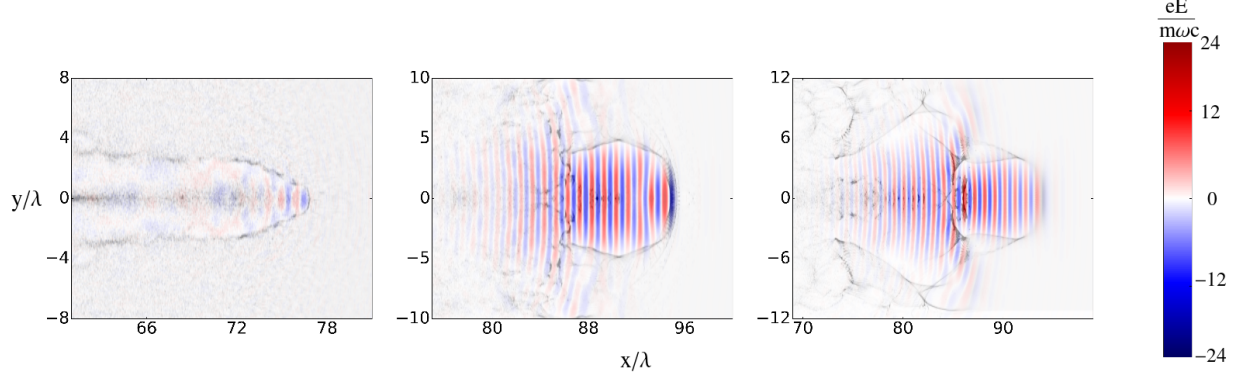


FIG. 2: Laser-plasma images for different electron densities $n_e = n_c$, $n_e = 0.1n_c$, and $n_e = 0.05n_c$ (in the first, middle, and last panels) after pulse propagation over three Rayleigh lengths within a target for $R_L = 2\lambda$ and $a_0 = 24$.

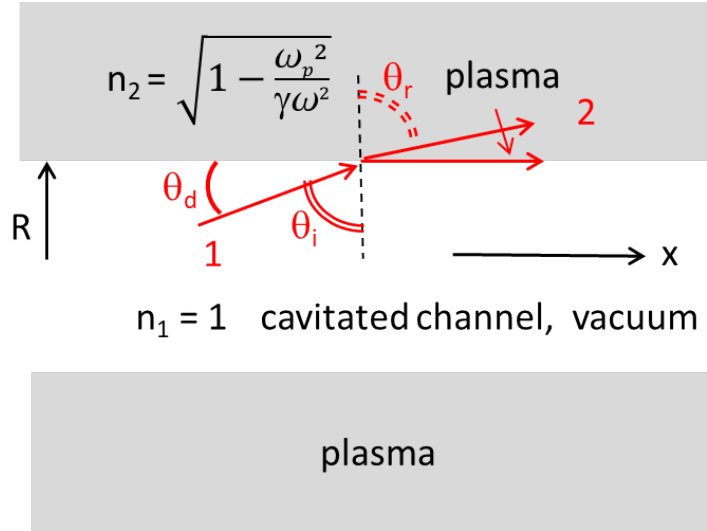


FIG. 3: Explanatory scheme for the self-trapped propagation of an intense light pulse.

consideration to the laser pulse propagation in a piecewise-inhomogeneous medium with a cylindrical channel (cavity) around the axis and plasma outside. In the cavity, light naturally diffracts with a typical angle $\theta_d \simeq \lambda/\pi R$, which defines an angle of incidence $\theta_i = \pi/2 - \theta_d$, as shown in Fig. 3. Snell's law $n_1 \sin \theta_i = n_2 \sin \theta_r$ governs the behavior of light rays as they propagate across an interface between two media (medium 1: vacuum with $n_1 = 1$; medium 2: plasma with $n_2 = \sqrt{1 - \omega_p^2/\gamma\omega^2}$) and defines the condition $\theta_r = \pi/2$ of the total

internal reflection, which requires

$$\theta_d^2 \simeq \left(\frac{2c}{\omega R} \right)^2 \simeq \frac{\omega_p^2}{\gamma \omega^2} \simeq \frac{\sqrt{2} \omega_p^2}{a_0 \omega^2} \quad (3)$$

for pulse propagation with an almost self-sustaining cavity radius. Here, we use $\gamma = \sqrt{1 + a_0^2/2} \simeq a_0/\sqrt{2}$. From Eq. (3), we easily obtain Eq. (1), where $\alpha = 2^{0.75}$, which is between the values assumed in Refs. [15, 18] ($\alpha = 1.12$) and in Refs. [4, 16] ($\alpha = 2$).

Because of strong diffraction, radii smaller than given by Eqs. (1) and (2) do not support self-channeled propagation of a laser beam, while filamentation makes a wider laser pulse unstable. The necessary condition for the absence of filamentation is that the laser pulse must initially be sufficiently narrow. Filaments cannot appear only if the laser pulse is not wider than the plasma skin length $R > (c/\omega_{pe})\sqrt{a_0}$ (see Eq. (1)). We note that condition (1) also corresponds to the force balance, where the ponderomotive force is counterbalanced by the radial electrostatic focusing force due to the ion cavity charge. By the above arguments, we can identify the propagation regime with the matched pulse spot size given by Eq. (1) as the most reliable for stable pulse propagation, which is expected to provide the highest current of accelerated electrons because pulse propagation is stable over a long distance. A regime of practically unchanged transverse laser beam size (i.e., a self-trapping regime) is known in relativistic self-focusing theory, which gives Eq. (1), where $\alpha = \sqrt{2}$ in the paraxial ray approximation with a simplified relativistic nonlinearity [19]. We note that the condition of complete electron cavitation immediately at the entrance of the light beam into the target also requires the same pulse radius in accordance with the most advanced theory, where self-focusing is associated with plasma nonlinearities due to both relativistic electron mass variation and relativistic charge displacement [20].

Our simulations demonstrate stable low-dissipation pulse propagation through many Rayleigh lengths, $X_R = \omega R_L^2/c$, in the form of self-trapped light ($L > D$, $L \gg \lambda_p/2$), as shown in Fig. 4. The laser field is shown in red-blue colors. There is also the longitudinal electrostatic field within laser cavities. It has a form of a single-cycle field with the wavelength equal to the cavity length L . The single-cycle electrostatic plasma field is strongly modulated because of the significant electron charge of the electron microbunches in the laser field with a λ -scale spacing. The longitudinal electrostatic field E in the laser cavity exceeds the Tajima–Dawson value ($E_{TD} = m_e \omega_p c/e$): $E = 4.5 E_{TD} \simeq 4.5 \text{ TV/m}$.

For the parameters used, the pulse propagation regime corresponds well to condition (1).

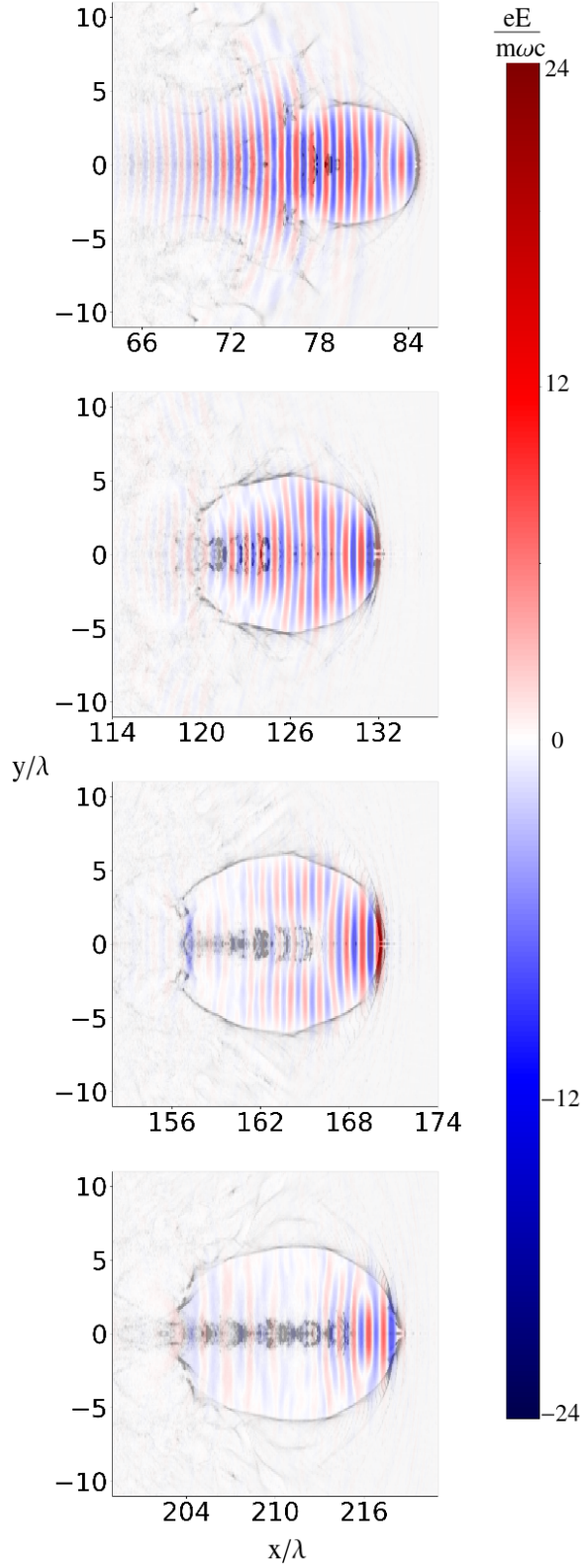


FIG. 4: Laser pulse propagation for optimum condition Eq. (1) ($a_0 = 24$, $R_L = 2\lambda$, $n_e = 0.1n_c$).

The formed laser cavity propagates ten Rayleigh lengths ($\sim 250\lambda$) for $a_0 = 24$, $R_L = 2\lambda$,

and $n_e = 0.1n_c$ from entering the plasma to the distance where the pulse depletes. We found that the estimate of the characteristic depletion scale $L_d \approx Ln_e/n_c \simeq 90\lambda$ from the effect of pulse depletion [21] agrees with our simulation result similar to that in Ref. [16]. This depletion is clearly seen in Fig. 4 and is expressed as a smooth shrinking of the pulse length to almost a single wavelength. Until the instant this happens, a plasma cavity is well pronounced, as seen Fig. 4, where the relative electron density is represented as different gray levels (darker denotes denser).

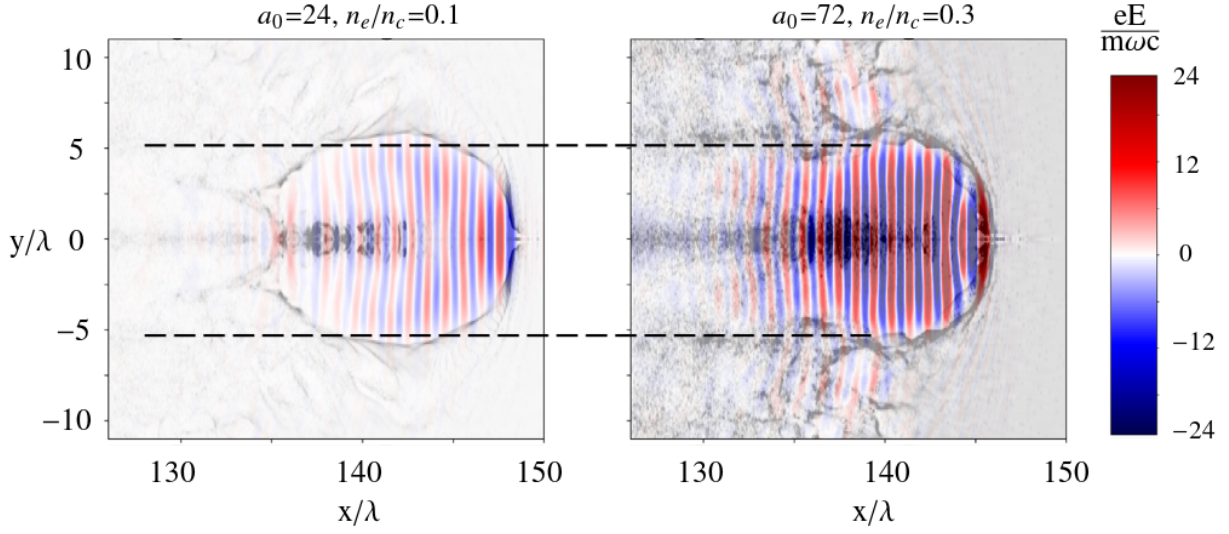


FIG. 5: Comparison of two self-trapping pulses with initial radius $R_L = 2\mu\text{m}$ and amplitudes $a_0 = 24$ (left) and $a_0 = 72$ (right) propagating in plasmas with the corresponding electron densities $0.1n_c$ and $0.3n_c$.

Matching condition (1), which corresponds to the most stable laser pulse propagation in the self-trapping regime and the maximum charge of high-energy electrons was also checked in PIC simulations by varying the laser field amplitude and laser hot spot size. Figure 5 clearly demonstrates preservation of the laser pulse size with a constant ratio a_0/n_e . If the laser focal spot size doubles from $R_L = 2\mu\text{m}$ to $R_L = 4\mu\text{m}$, then the size of the self-steady accelerating structure also doubles and becomes $R = 10\mu\text{m}$. The optimal plasma density correspondingly decreases ~ 4 to 5 times in accordance with Eq. (1), which demonstrates the validity of this matching condition for another radius R . This is illustrated in Fig. 6.

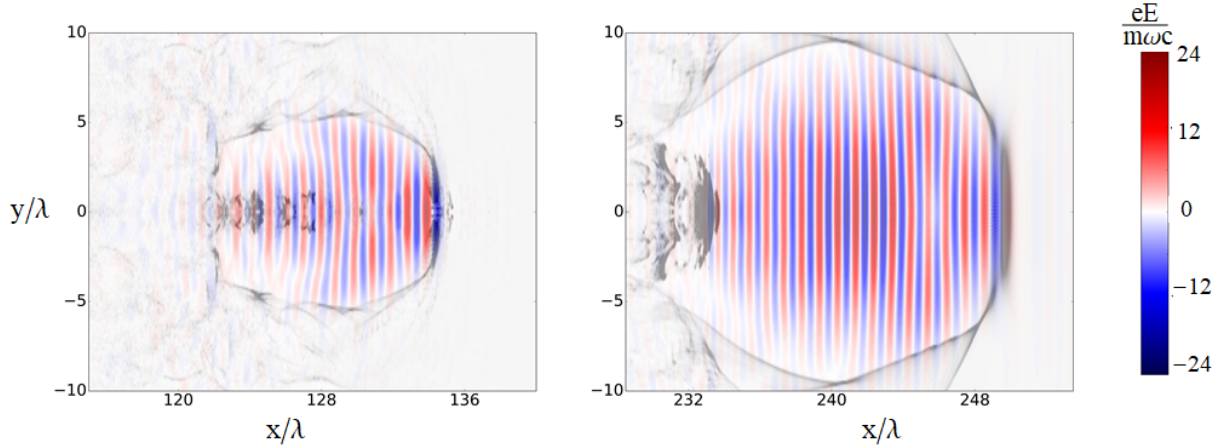


FIG. 6: Comparison of two self-trapping pulses with the amplitude $a_0 = 24$ and initial radii $R_L = 2 \mu\text{m}$ (left) and $R_L = 4 \mu\text{m}$ (right) propagating in plasmas with the corresponding electron densities $0.1n_c$ and $0.02n_c$.

IV. ELECTRON ACCELERATION

In our simulations, we collect all the electrons escaping in the forward direction behind the target in vacuum with energy greater than 30 MeV. For example, such electrons can be used to generate MeV gammas from a converter target of high atomic charge number (see Fig. 1). For each given laser power, we performed several runs in the vicinity of Eq. (1) to maximize the total charge Q of high-energy electrons. Such maximization also includes a proper choice of the target length $l \simeq 2L_d$ to $3L_d$, i.e., about the length of entire pulse depletion.

The detected charges of high-energy electron bunches with energies greater than 30 MeV behind a target are shown in Fig. 7 for three values of power. The electron acceleration scenario is quite different from the bubble wakefield regime, which requires a laser pulse length less than the plasma wavelength, $\lambda_p = 2\pi c/\omega_{pe}$, where ω_{pe} is the electron plasma frequency. The laser pulse does not excite a plasma wave behind it. At the same time, the laser pulse is too short to excite plasma waves driven by forward stimulated Raman scattering (FSRS) [22].

Ambient electrons flow into the accelerating cavity from its backside similarly to the standard bubble wakefield case because laser field is weakened at the pulse tail. These electrons enter strong laser and plasma fields and accelerate quickly to the speed of light. They

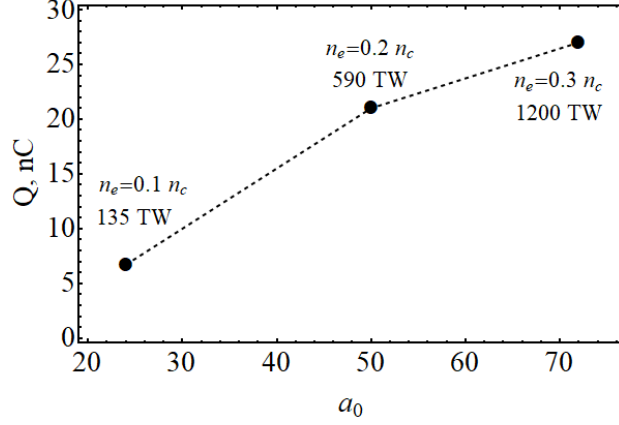


FIG. 7: The maximum total charge of electron bunches for electrons accelerated in the laser self-trapping regime to energies > 30 MeV.

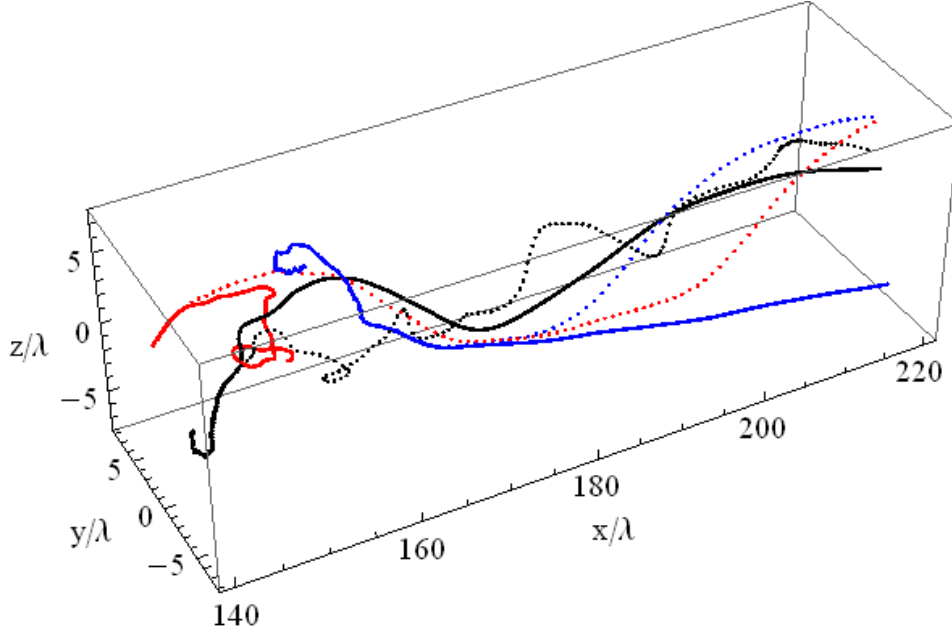


FIG. 8: Comparison of how 10^{-4} perturbations affect the behavior of several electron trajectories: the reference trajectories are shown by solid lines and the perturbed trajectories are shown by dotted lines.

co-propagate with the laser pulse and electrostatic field for a rather long time, but the laser field is finally depleted during propagation, and the particle motion becomes increasingly dominated by the longitudinal electrostatic field. The pre-acceleration mechanism of the electrons could be called a specific kind of direct laser acceleration enabling an effective loading of a large number of particles into the accelerating electrostatic plasma field. An

amplitude modulation of such a single-cycle electrostatic field also contributes stochastically to the occurrence of electron acceleration similarly to that observed for FSRS [23].

The stochastic nature of electron loading can be proved by the following simulation trick, which replaces the more complicated Lyapunov exponent analysis [23]. We compared electron trajectories with those from an additional run in which we studied the system stability by adding small momentum perturbations ($|\delta\mathbf{p}|/p = 10^{-4}$) for some electrons at a given instant in the initial stage of electron pre-acceleration, similarly to what was done in Ref. [24]. Figure 8 compares the electron trajectories with and without perturbations and shows the significant difference in the final particle trajectories, proving the stochastic nature of the electron acceleration.

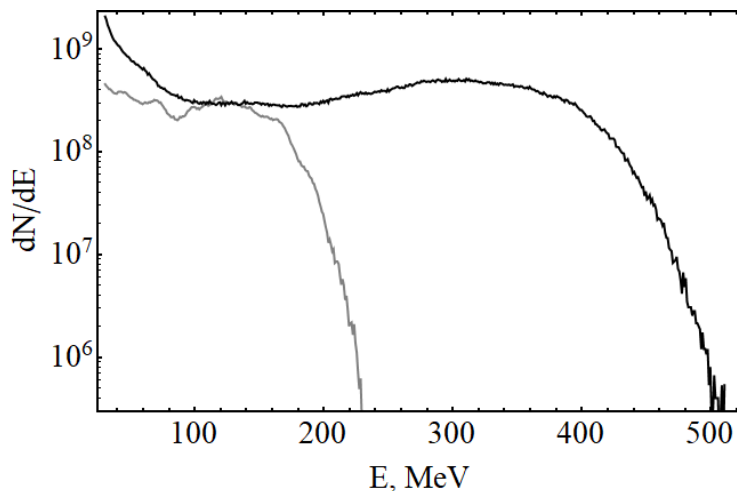


FIG. 9: Energy spectra of high-energy (> 30 MeV) electrons that left the target: they correspond to the two laser powers in Fig. 5, $P = 135$ TW (gray curve) and 1200 TW (black curve).

The spectra of accelerated electrons in the self-trapping regime from low-density targets show their enrichment by high-energy particles. The electron spectra have a well-pronounced energy plateau, as can be seen in Fig. 9. Such flattened distributions are formed from accelerating electrons of modest energies and high-energy electrons that are already dephased with respect to the electrostatic field and are decelerating. Introducing an effective temperature T_h as the ratio of the total bunch energy to the total number of electrons in the bunch (see Fig. 9), we correspondingly derive $T_h = 97$ MeV and $T_h = 210$ MeV for $P = 130$ TW and $P = 1200$ TW. The laser-to-electron beam energy conversion efficiency is $\sim 15\%$ for all laser energies considered above.

V. NUCLEAR EMISSION FROM BREMSSTRAHLUNG CONVERTER TARGET

Since the first proposals to use intense ultrashort laser pulses to trigger nuclear reactions appeared [25, 26], this issue has been overgrown with numerous original applications. Electron acceleration by a laser-excited plasma wakefield have been used to produce gamma rays by passing through high-Z material converters. This technique has distinct advantages over direct laser irradiation of solid targets because the source size is small. One of the first experiments on generating bremsstrahlung gamma rays from laser wakefield acceleration was reported in Ref. [27].

For high photon energies beyond several MeV, generation by bremsstrahlung is most attractive. It is typically produced when electrons accelerated in low density are converted to high-energy photons in a high-Z material. The gamma source size is rather small, which makes it potentially useful for gamma-ray radiography with a high spatial resolution. Gamma-ray radiography with a single shot is often very desirable. This allows the users to have gamma-imaging with a high temporal resolution. Certainly, only high-brightness sources can work in this way, and the highest possible charge of the accelerated electrons is required.

Significant developments in the laser acceleration of electrons to energies exceeding 100 MeV have enabled tabletop photonuclear physics to be explored. Such energetic electron beams have an array of applications in radioisotope production, photofission induction, neutron generation, electron-positron pair generation, and even possibly light meson production. The latter was already demonstrated experimentally [28]. A laser-driven neutron source has a very short temporal scale, which is favorable for applications that use pulsed neutron sources, for example, fast neutron resonance radiography [29]. In our numerical simulations (see Fig. 1), we use a high-charge electron bunch to irradiate high-Z material with the aim to produce both gamma rays and photonuclear reactions with a high yield.

A. Generation of gamma rays

An electron bunch accelerated by a short pulse in a laser target was used for bremsstrahlung production of gamma rays from the second target (high-Z converter target) placed immediately behind the laser target. Using the Monte Carlo simulation tool

GEANT4, we calculated the total yield of gamma rays emitted from a Pt target (of natural composition, $^{194}\text{Pt}+^{195}\text{Pt}+^{196}\text{Pt}+^{198}\text{Pt}$) of different thicknesses, the gamma energy spectrum, and the angular distribution of gamma rays for a 100 TW laser pulse.

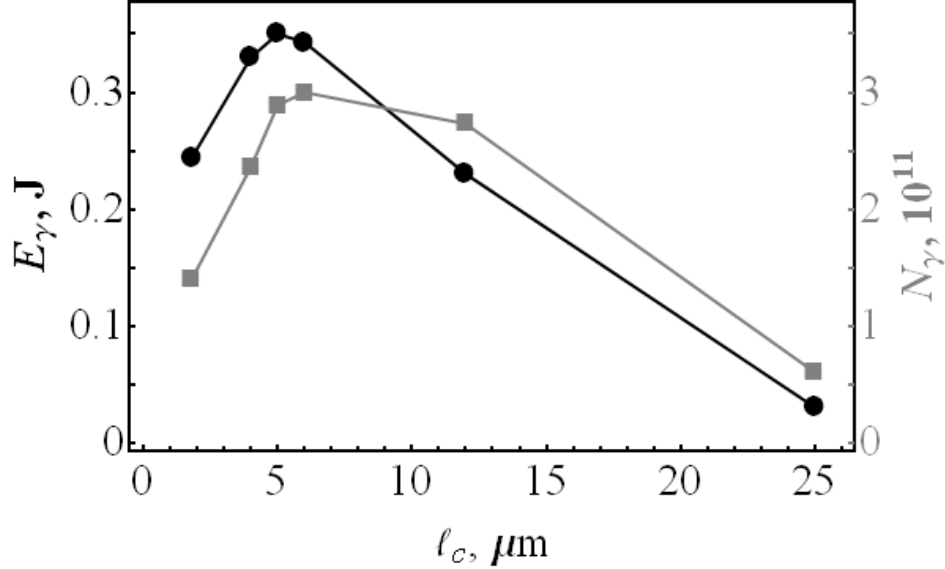


FIG. 10: Total yield (left) and energy (right) of gamma rays versus the thickness l_c of the Pt converter target for the laser-plasma parameters $P = 130$ TW, $R_L = 2\lambda$, and $n_e = 0.1n_c$ corresponding to an electron bunch with $Q \simeq 7$ nC and an average energy 100 MeV.

The total yield and energy of gamma photons leaving the converter target as a function of its thickness are shown in Fig. 10. The maximum gamma yield (MGY) converter has a thickness ~ 5 to 6 mm, which somewhat exceeds the electron stopping length of 100 MeV particles in Pt (~ 3 mm), i.e., such a converter target stops the electrons almost entirely and is transparent for MeV gamma radiation. The maximum total yield of MeV gamma radiation is as high as 3×10^{11} photons, ~ 0.35 J. Correspondingly, this gives $\sim 8\%$ laser-to-gamma conversion efficiency, which is much higher than 3D PIC–Monte Carlo simulations predict for gamma bremsstrahlung production from ultraintense femtosecond laser–solid interactions with front surface structures [30] or with a lengthy plasma corona [31]. A gamma ray source based on bremsstrahlung radiation generated by wakefield accelerated electrons in a rarefied plasma [32] is also noncompetitive relative to the considered regime because the electron charge is significantly lower.

Figure 11 illustrates a spectral distribution of the generated gamma rays of multi-MeV energy with a strong dominance of their production in the forward direction and the energy-

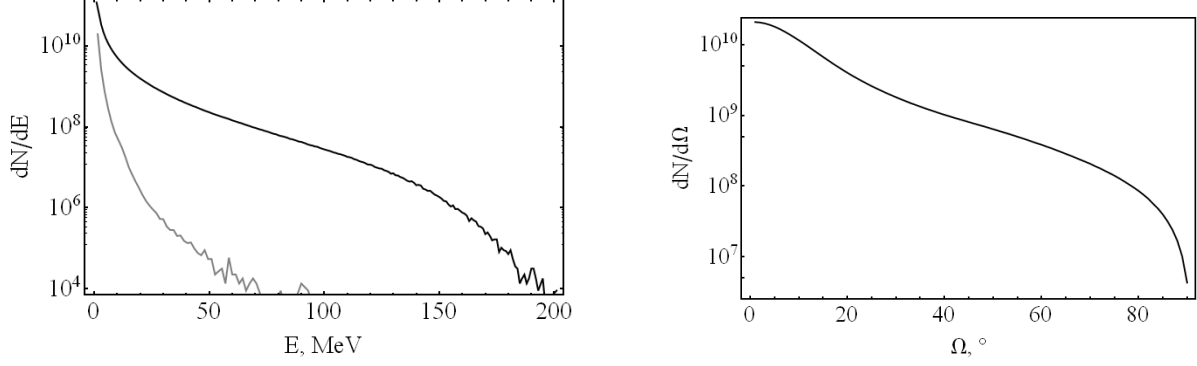


FIG. 11: Energy spectra (left panel) and angular distribution of gamma rays generated from a 6 mm thick Pt target in the forward (black) and backward (gray) directions for the laser-plasma parameters $P = 130$ TW, $R_L = 2\lambda$, and $n_e = 0.1n_c$ corresponding to an electron bunch with $Q \simeq 7$ nC and average energy 100 MeV.

integrated angular distribution of gamma rays (left and right panels). The energy spectrum shows a two-temperature distribution of gamma rays with $T_\gamma \simeq 2.5$ MeV for MeV gamma rays and $T_\gamma \simeq 25$ MeV for photons with energies exceeding 30 MeV. The energy of high-temperature gamma photons is ~ 0.1 J.

To estimate the gamma ray brightness, we use the duration and spot size of gamma rays from the GEANT4 simulation. Both the duration and spot radius depend weakly on the gamma energy but depend strongly on the converter target thickness. For the MGY converter target of 5 to 6 mm thickness, they are 0.3 ps and $60 \mu\text{m}$. These values are much higher than the electron beam duration (~ 30 fs) and size ($\sim 5 \mu\text{m}$) often used to estimate the gamma brightness (see, e.g., [30]). For the corresponding divergence 10° in the simulation, we obtain $\simeq 5 \times 10^{17} \text{s}^{-1} \text{mrad}^{-2} \text{mm}^{-2} (0.1\% \text{BW})^{-1}$ for the 10 MeV gamma brightness. On the other hand, for the thinner target (1.8 mm thickness), which produces a gamma pulse of 100 fs duration and $17 \mu\text{m}$ spot radius, the 10 MeV gamma brightness increases more than an order of magnitude to $\sim 10^{19} \text{s}^{-1} \text{mrad}^{-2} \text{mm}^{-2} (0.1\% \text{BW})^{-1}$ despite the considerable reduction in the total number of generated gamma photons (see Fig. 10). The brightness of the 100 MeV gamma source is approximately an order of magnitude less than the above estimates.

B. Photoproduction of electron–positron pairs

Our next GEANT4 simulations were performed to study electron–positron pair production with a 100 TW laser pulse. The electron beam was acting on the same Pt slab of 6 mm thickness, which also maximizes positron yield. The positrons were considered when escaping from the backside of this target. The thicker target gives fewer electrons and positrons escaping from it. The bremsstrahlung emission of photons by electrons and the creation of electron–positron pairs by photons are the dominant processes leading to the generation of the detected electron–positron jet (see the right panel in Fig. 12).

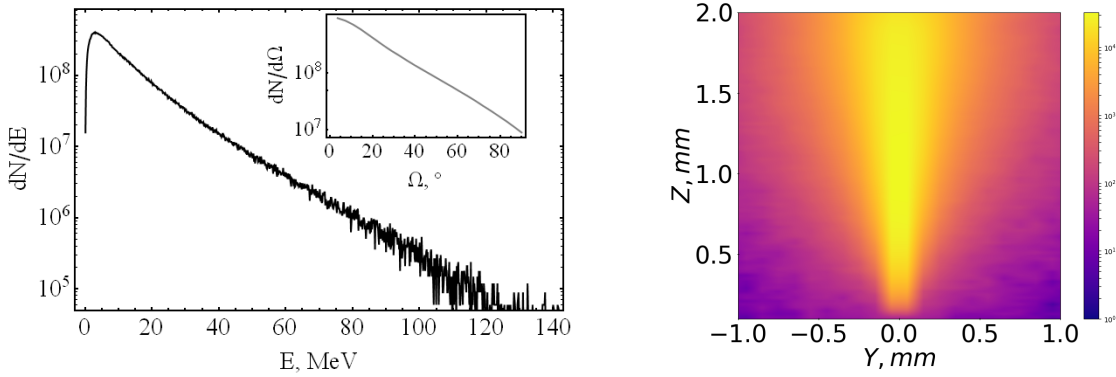


FIG. 12: Energy spectrum of positrons generated from a 6 mm Pt target (left panel) and positron flux in a 1.8 mm Pt target (right panel) for the laser–plasma parameters $P = 130$ TW, $R_L = 2\lambda$, and $n_e = 0.1n_c$ corresponding to an electron bunch with $Q \simeq 7$ nC and average energy 100 MeV. The inset in left panel shows the angular distribution of positrons generated from the 6 mm Pt target.

We compared positron distributions for converter targets of different thicknesses. A thickness increase results in angular blurring of generated positrons. A better collimated positron jet results from a thin target (shown inside a converter the right panel in Fig. 12). The positron jet angular spread increases from $\sim 20^\circ$ for a 1.8 mm Pt converter target to $\sim 35^\circ$ for a 6 mm target and $\sim 40^\circ$ for a 12 mm target. The spectrum of positrons from a 6 mm Pt target is shown in Fig. 12. Simulations show that majority of positrons are produced with an energy of the order of a few MeV, which corresponds well to a Jüttner–Synge distribution [33]. The total number of generated positrons is 9×10^9 , which is higher than observed in Ref. [34]. But the energy was lower there because more energetic electrons were

generated in Ref. [34]. The 6 mm thick Pt target produces the maximum number of positrons. Because such a relatively thin target is unable to stop all electrons from the injected electron beam, the total number of electrons behind the converter target is an order of magnitude higher than the number of positrons. Increasing the Pt target thickness to 24 mm results in an almost neutral electron–positron hot plasma jet behind the converter with the total number of particles of two orders of magnitude less than in the optimum thickness case. We note that in this case, there is a large number of low-energy electrons appearing due to secondary processes like Compton, Moller, and Bhabha scattering accounted for in the GEANT4 code.

C. Photonuclear production of neutrons

Photonuclear production of neutrons is a widely discussed topic in nuclear applications of short-pulse intense lasers. One scheme is to irradiate the converter with high-energy electron beams from laser wakefield acceleration [35, 36]. We discuss this here using the self-trapping regime. Such a regime enables generation of gamma rays with energies exceeding 10 MeV. This gamma energy range is well suited for photonuclear neutron production through the giant dipole resonance (GDR). The isovector GDR is known as the fundamental collective nuclear excitation [37]. The GDR can be understood macroscopically as a bulk nuclear vibration where protons with isospin $T_3=1/2$ and neutrons with isospin $T_3=-1/2$ oscillate coherently in opposite directions. Coherent excitation makes a sufficiently large cross section. In general, the photonuclear cross section is smaller than typical nuclear cross sections because of the electromagnetic nature of the interaction. Nevertheless, at resonance energy, it is comparable in order of magnitude to the geometric nuclear cross section, which well compensates the weak electromagnetic interaction. It is larger than the most (n, γ) cross sections.

Photonuclear cross sections typically have broad peaks with relatively high values in the GDR energy region 10 to 20 MeV. This is the case with the gamma source presented in Sec. V A (see Fig. 8). The photonuclear reactions at the GDR region are mainly $(\gamma, 2n)$ and to a lesser extent (γ, n) , although Geant4 (version 10.5), which is well suited for selected GDR cross sections, also simulates a variety of reactions: (γ, n) , $(\gamma, 2n)$, (γ, np) , $(\gamma, 3n)$, and so on. We note that the secondary gamma radiation emitted by excited nuclei are also

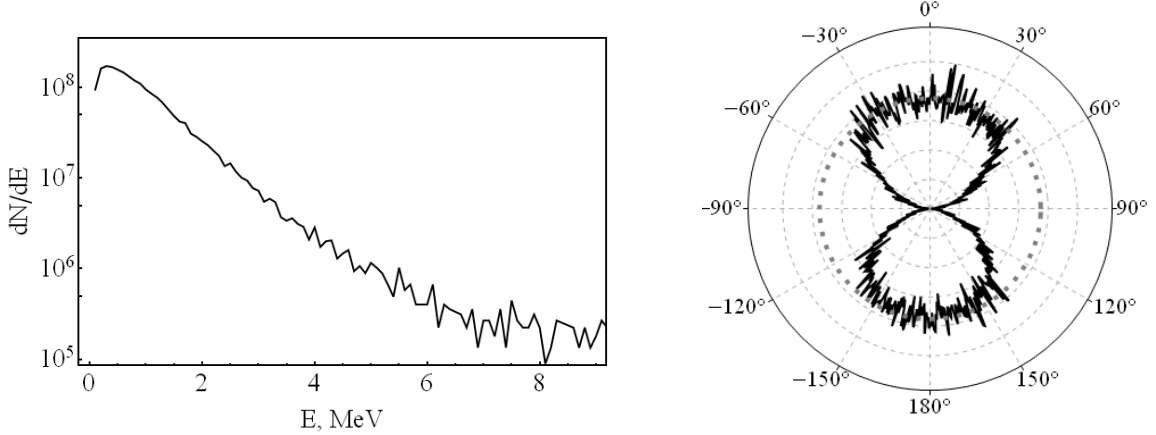


FIG. 13: Energy spectrum (left panel) and angular distribution (right panel) of neutrons generated from a 12 mm thick Pt target outside the target in the forward and backward directions (in a 108° angle in both cases) for the same laser-plasma parameters as in Fig. 11.

taken into account in Geant4 simulations.

The results for photonuclear neutron production with a 130 TW laser are shown in Fig. 13. The maximum number of generated neutrons from a Pt target with a 12 mm thickness reaches 2×10^8 particles. It roughly corresponds to a 5×10^{-3} electron-neutron conversion efficiency [38]. Using the 6 mm Pt target (which maximizes gamma and positron yields) cuts the neutron number in half compared with the considered 12 mm Pt target. The thicker converter target is needed for neutron production because the photonuclear (n, γ) cross section is much less than the positron production cross section and a longer propagation distance is hence required. The generated neutrons have an almost isotropic distribution and exponential-like spectrum with a temperature ~ 1 MeV. Because we collect only particles moving in forward and backward directions outside the converter target (in a 108° angle), the angular distribution in Fig. 13 (right panel) does not contain cross-side generated neutrons. It shows some small forward-backward anisotropy. The number of forward-produced neutrons exceeds the number of backward ones by approximately 10%.

D. Photoproduction of pions

Pions are light mesons (consisting of quarks and antiquarks) with a rest mass of 140 MeV. They are a key decay product in high-energy particle physics experiments. Despite having a

larger rest mass than muons, they require less energy (threshold energy is 140 MeV) to appear with gamma-produced (virtual) quark–antiquark pairs in nuclei than for electromagnetic production of muon–antimuon pairs (the required energy is 212 MeV).

For gamma energies up to 1 GeV, there are two main channels of pion generation: excitation of baryon resonances and direct (nonresonant) single pion production, i.e., due to quark extraction from the nucleus (neutron or proton). The direct two-body channel $\gamma N \rightarrow \pi N$ dominates near a threshold up to a gamma energy of 200 to 300 MeV. For higher energies, the photon wavelength becomes comparable to the nucleon radius, and photons mainly interact with single nucleons by exciting baryon resonances. The excitation of the three baryon resonances $\Delta(1232)$, $N^*(1520)$, and $N^*(1680)$ is the most important. The lifetime of these resonances are less than 10^{-23} s (e.g., the lifetime of the $\Delta(1232)$ resonance is 5.6×10^{-24} s). The resonances commonly decay with pion production. In the case of a 135 TW laser pulse, the maximum electron beam energy is only slightly above the pion production threshold (see Fig. 7), and this results in a small number of photons with near-threshold energies of 140 MeV. Therefore, our simulation predicts the generation of only about 150 pions of different species (π^+ , π^- , and π^0). This number is comparable to the experimental results in Ref. [28], where only direct pion production was detected. The total number of generated pions dramatically increases for a 1200 TW laser pulse. It reaches $\sim 10^6$ for each pion species). The spectra of π^+ and π^- pions are presented in Fig. 14.

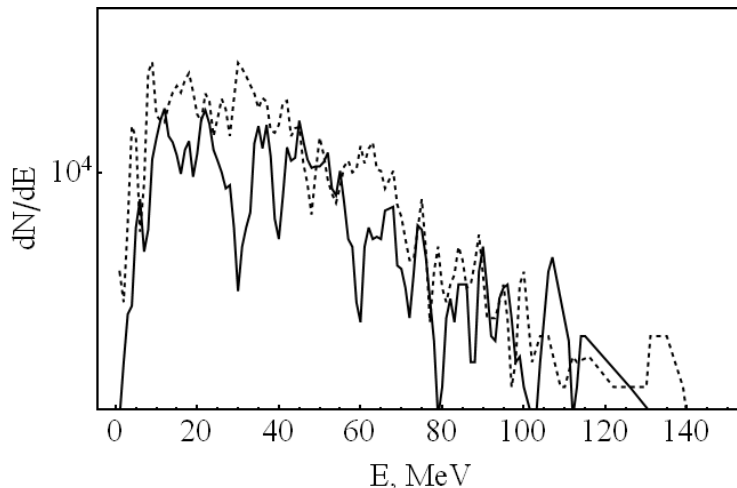


FIG. 14: Spectra of photonuclear generated π^+ (solid line) and π^- (dashed line) pions for a 1200 TW laser pulse.

The lifetime of the π^0 pion is 8.4×10^{-17} s and it decays (with a probability 0.98823) to two gamma photons. The lifetime of the π^\pm pions is 26 ns, and they decay (with a probability 0.999877) to the corresponding μ^\pm muons. These decays are the main channel of muon production in our case. For direct muon production due to photon–nucleus interaction, the higher photon energies and correspondingly higher electron beam energies are required. This agrees with the prediction in Ref. [39], where direct muon production was numerically observed with a multi-GeV electron beam from laser wakefield acceleration.

VI. CONCLUSIONS

We have performed 3D PIC simulations using the code VSim to model electron acceleration in low-density targets with lasers of intensities from 0.8 to 7×10^{21} and powers from 135 to 1200 TW subsequently complemented by Monte Carlo simulations using the code GEANT4 to model gamma, positron, and photonuclear particle production. We considered the self-trapping regime of relativistic laser channeling in a near-critical plasma, which enables stable laser pulse propagation over many Rayleigh lengths. This regime is the most suitable for photonuclear reactions because it can provide the maximum total charge (multi-nC) of electrons accelerated to a hundred MeV with current short-pulse intense lasers. For PW class lasers, the electron bunch charge can be as high as several tens of nC.

The considered self-trapping regime of laser pulse propagation corresponds to the matched pulse spot size given by Eq. (1). This is a regime of practically unchanged transverse laser beam size. The corresponding nonlinear structure looks like an empty cavity of pulse length with an electrostatic field filled with a laser field (a “laser bullet”). The considered relativistic laser pulse satisfies the condition of complete electron cavitation immediately at the entrance of the light into the target, which supports almost the same pulse radius over entire propagation length until pulse depletion in accordance with the most advanced theory, where self-focusing is associated with plasma nonlinearities due to both relativistic electron mass variation and relativistic charge displacement [20]. Acceleration of electrons in laser bullet occurs as a combination of direct laser acceleration and electrostatic wake acceleration with a stochastic feature. The electron energy spectra show a well-pronounced plateau of the width $\Delta E \sim E \sim 100$ to 300 MeV (see Fig. 9).

One possible application of the proposed acceleration scheme is to generate gamma quanta

with characteristic energies up to tens of MeV via bremsstrahlung emission by electrons passing through a heavy metal converter plate placed behind the laser target. Such gamma radiation can be used for radiography of dense samples a few tens of centimeters thick, which is in great demand for materials science and security inspections. With a 130 TW 30 fs laser pulse, for example, we obtained an electron–photon conversion efficiency at the level of 5% for ~ 2.5 MeV gamma photons and 2% for ~ 25 MeV gamma photons. The estimated brightness of 10 MeV gamma rays is $\sim 10^{19}\text{s}^{-1}\text{mrad}^{-2}\text{mm}^{-2}(0.1\%\text{BW})^{-1}$. We estimated the photo-production yield of neutrons, positrons, and pions, which is also benefited by the high charge of the generated electron beam in the self-trapping regime of the laser pulse. While the low repetition rate of high-energy laser facilities has limited the development of photo-nuclear sources, several multi-Joule and multi-Hz laser systems will become available over the next five years. Our study highlights the potential of high-repetition rate experiments by demonstrating the advantage of near-critical gas targets.

VII. ACKNOWLEDGMENTS

This work was supported by the Russian Science Foundation (Grant No. 17-12-01283).

-
- [1] T. Tajima and J. M. Dawson, Phys. Rev. Lett. **43**, 267 (1979).
 - [2] E. Esarey, P. Sprangle, J. Krall, and A. Ting, IEEE Trans. Plasma Sci. **24**, 252 (1996).
 - [3] A. Pukhov and J. Meyer-ter-Vehn, Appl. Phys. B: Lasers Opt. **74**, 355 (2002).
 - [4] M. G. Lobok, A. V. Brantov, D. A. Gozhev, and V. Yu. Bychenkov Plasma Phys. Control. Fusion **60**, 084010 (2018).
 - [5] Y. Yang, J. Jiao, C. Tian, Y. Wu, K. Dong, W. Zhou, Y. Gu, and Z. Zhao, Laser and Particle Beams **35**, 476 (2017).
 - [6] L. Willingale, P. M. Nilson, A. G. R. Thomas, S. S. Bulanov, A. Maksimchuk, W. Nazarov, T. C. Sangster, C. Stoeckl, and K. Krushelnick, Phys. Plasmas **18**, 056706 (2011).
 - [7] A. J. Goers, G. A. Hine, L. Feder, B. Miao, F. Salehi, J. K. Wahlstrand and H. M. Milchberg, Phys. Rev. Lett. **115**, 194802 (2015).
 - [8] F. Albert and A. G. R. Thomas, Plasma Phys. Control. Fusion **58**, 103001 (2016).

- [9] J. Wenz, S. Schleede, K. Khrennikov, M. Bech, P. Thibault, M. Heigoldt, F. Pfeiffer, S. Karsch, Nat. Commun. **6**, 7568 (2015).
- [10] C. Courtois, R. Edwards, A. Compant La Fontaine, C. Aedy, S. Bazzoli, J. L. Bourgade, J. Gazave, J. M. Lagrange, O. Landoas, L. Le Dain, D. Mastrosimone, N. Pichoff, G. Pien, and C. Stoeckl, Phys. Plasmas **20**, 083114 (2013).
- [11] C. M. Brenner, S. R. Mirfayzi, D. R. Rusby, C. Armstrong, A. Alejo, L. A. Wilson, R. Clarke, H. Ahmed, N. M. H. Butler, D. Haddock, Plasma Phys. Control. Fusion **58**, 014039 (2016)
- [12] W. Luo, M. Bobeica, I. Gheorghe, D. M. Filipescu, D. Niculae and D. L. Balabanski, Appl. Phys. B **122**, 8 (2016)
- [13] S. A. Reed, V. Chvykov, G. Kalintchenko, T. Matsuoka, P. Rousseau, V. Yanovsky, C. R. Vane, J. R. Beene, D. Stracener, D. R. Schultz, A. Maksimchuk, Appl. Phys. Lett. **89**, 231107 (2006)
- [14] G. Mourou, Z. Chang, A. Maksimchuk, J. Nees, S. V. Bulanov, V. Yu. Bychenkov, T. Zh. Esirkepov, N. M. Naumova, F. Pegoraro, H. Ruhl, Plasma Phys. Rep. **28**, 12 (2002).
- [15] S. Gordienko and A. Pukhov, Phys. Plasmas **12**, 043109 (2005).
- [16] W. Lu, M. Tzoufras, C. Joshi, F. S. Tsung, W. B. Mori, J. Vieira, R. A. Fonseca, and L. O. Silva, Phys. Rev. ST Accel. Beams **10**, 061301 (2007).
- [17] G.-Z. Sun, E. Ott, Y. C. Lee, and P. Guzdar, Phys. Fluids **30**, 526 (1987).
- [18] K. I. Popov, W. Rozmus, V. Yu. Bychenkov, N. Naseri, C. E. Capjack, and A. V. Brantov, Phys. Rev. Lett. **105**, 195002 (2010).
- [19] K. Walia and A. Singh, Contrib. Plasma Phys. **51**, 375 (2011).
- [20] V. F. Kovalev, and V. Yu. Bychenkov, Phys. Rev. E **99**, 043201 (2019)
- [21] C. D. Decker, W. B. Mori, K. C. Tzeng and T. Katsouleas, Phys. Plasmas **3**, 2047 (1996).
- [22] P. Sprangle and E. Esarey, Phys. Fluids **4**, 2241 (1992).
- [23] S. G. Bochkarev, A. V. Brantov, V. Yu. Bychenkov, D. V. Torshin, V. F. Kovalev, G. V. Baidin and V. A. Lykov, Plasma Phys. Reports **40**, 202 (2014).
- [24] Y. Sentoku, V. Yu. Bychenkov, K. Flippo, A. Maksimchuk, K. Mima, G. Mourou, Z. M. Sheng, and D. Umstadter, Appl. Phys. B **74**, 207 (2002).
- [25] V. Yu. Bychenkov, V. T. Tikhonchuk and S. A. Tolokonnikov, JETP **88**, 1137 (1999).
- [26] K. W. D. Ledingham and P. A. Norreys, Contemp. Phys. **40**, 367 (1999).
- [27] R. D. Edwards, M. A. Sinclair, and T. J. Goldsack, K. Krushelnick, F. N. Beg, E. L. Clark,

- A. E. Dangor, Z. Najmudin, M. Tatarakis, B. Walton, and M. Zepf, K. W. D. Ledingham and I. Spencer, P. A. Norreys, R. J. Clarke, R. Kodama, Y. Toyama, and M. Tampo, Appl. Phys. Lett. **80**, 2129 (2002).
- [28] W. Schumaker, T. Liang, R. Clarke, J. M. Cole, G. Grittani, S. Kuschel, S. P. D. Mangles, Z. Najmudin, K. Poder, G. Sarri, D. Symes, A. G. R. Thomas, M. Vargas, M. Zepf, and K. Krushelnick, New J. Phys. **20**, 073008 (2018).
- [29] I. Mor, D. Vartsky, D. Bar, G. Feldman, M. B. Goldberg, D. Katz, E. Sayag, I. Shmueli, Y. Cohen, A. Tal, JINST **4**, P05016 (2009).
- [30] S. Jianga, A. G. Krygier, D. W. Schumacher, K. U. Akli, and R. R. Freeman, Eur. Phys. J. D **68**, 283 (2014).
- [31] M. G. Lobok, A. V. Brantov, and V. Yu. Bychenkov, Quantum Electronics **47**, 232 (2017).
- [32] S. Cipiccia, S. M. Wiggins, R. P. Shanks, M. R. Islam, G. Vieux, R. C. Issac, E. Brunetti, B. Ersfeld, G. H. Welsh, M. P. Anania, D. Maneuski, N. R. C. Lemos, R. A. Bendoyro, P. P. Rajeev, P. Foster, N. Bourgeois, T. P. A. Ibbotson, P. A. Walker, V. O. Shea, J. M. Dias, and D. A. Jaroszynski, J. Appl. Phys. **111**, 063302 (2012).
- [33] J. L. Synge, The Relativistic Gas (North-Holland Pub. Co. 1957)
- [34] G. Sarri, K. Poder, J.M. Cole, W. Schumaker, A. Di Piazza, B. Reville, T. Dzelzainis, D. Doria, L.A. Gizzi, G. Grittani, S. Kar, C.H. Keitel, K. Krushelnick, S. Kuschel, S.P.D. Mangles, Z. Najmudin, N. Shukla, L.O. Silva, D. Symes, A.G.R. Thomas, M. Vargas, J. Vieira, and M. Zepf, Nature Comm. **6** 6747 (2015).
- [35] S. A. Reed, V. Chvykov, G. Kalintchenko, T. Matsuoka, V. Yanovsky, C. R. Vane, J. R. Beene, D. Stracener, D. R. Schultz, and A. Maksimchuk, J. Appl. Phys. **102**, 073103 (2007).
- [36] X.J. Jiao, J.M. Shaw, T. Wang, X.M. Wang, H. Tsai, P. Poth, I. Pomerantz, L.A. Labun, T. Toncian, M.C. Downer, and B.M. Hegelich, Matter and Radiation at Extremes **2**, 296 (2017).
- [37] M. N. Harakeh and A. van der Woude *Giant Resonances: Fundamental High-Frequency Modes of Nuclear Excitation* (Oxford University Press Oxford 2001).
- [38] W. C. Barber and W. D. George, Physical Review **116**, 1551 (1959).
- [39] B. S. Rao, J H Jeon, H. T. Kim and C. H. Nam, Plasma Phys. Control. Fusion **60**, 095002 (2018).